PCCP

ROYAL SOCIETY OF CHEMISTRY

PAPER

View Article Online
View Journal | View Issue

Cite this: *Phys. Chem. Chem. Phys.*, 2023, **25**, 7697

Mg(I)–Fe(−II) and Mg(0)–Mg(I) covalent bonding in the $Mg_nFe(CO)_4^-$ (n = 1, 2) anion complexes: an infrared photodissociation spectroscopic and theoretical study†

Xiaoyang Jin, Guanjun Wang and Mingfei Zhou *

Received 7th December 2022,
Accepted 16th February 2023

DOI: 10.1039/d2cp05719k

rsc.li/pccp

Heteronuclear magnesium–iron carbonyl anion complexes $MgFe(CO)_4^-$ and $Mg_2Fe(CO)_4^-$ are produced in the gas phase and are detected by mass-selected infrared photodissociation spectroscopy in the carbonyl stretching frequency region. The geometric structures and the metal–metal bonding are discussed with the aid of quantum chemical calculations. Both complexes are characterized to have a doublet electronic ground state with C_{3v} symmetry containing a Mg–Fe bond or a Mg–Mg–Fe bonding unit. Bonding analyses indicate that each complex involves an electron-sharing Mg(I)–Fe(−II) σ bond. The $Mg_2Fe(CO)_4^-$ complex involves a relatively weak covalent Mg(0)–Mg(I) σ bond.

Introduction

Molecular compounds containing metal–metal bonds have aroused considerable research interest for decades.[1–6] Metal–metal bonding is quite common for transition metals and p-block main group metals. However, the alkaline-earth elements are rarely involved in metal–metal bonding. Due to the electropositive nature, the alkaline earth metals readily lose the two valence *n*s electrons to form fully oxidized ionic compounds and are very reluctant to form covalent metal–metal bonds. Significant efforts have been made to synthesize and characterize metal–metal bonded compounds involving the alkaline earth elements,[7–42] among which magnesium is the most studied one for both the homonuclear and heteronuclear systems.[14–39]

The first dimeric Mg(I) compound (L)MgMg(L) stabilized by extremely bulky chelating anionic N-ligands was synthesized by Jones and coworkers in 2007.[14] Subsequently, a library of complexes containing the homonuclear Mg(I)–Mg(I) bond have been reported.[15–17] These magnesium(I) dimers are recognized as valuable reducing agents, capable of reductive C–C and N–N bond coupling, C–F, C–H, C–C and C=C bond activation or cleavage and CO reductive oligomerization.[18–26] Although initially classified as a normal covalent σ bond,[27] the Mg(I)–Mg(I) bond was later claimed to contain a non-nuclear attractor (NNA).[28] The Mg(I)–Mg(I) bond lengths in different dimeric Mg(I) compounds were measured to lie over a wide range.[29] The longest bond interaction (> 3.2 Å) so far was detected in the $[\{SiN^{Dipp}\}MgNa]_2$ complex, which was augmented by persistent Na-aryl interactions.[30] More than dimeric Mg(I) compounds, strongly reducing beta-diketiminate complexes containing magnesium in its zero oxidation state were isolated recently, among which a compound with a linear Mg_3 core that could formally be described as a Mg(I)–Mg(0)–Mg(I) unit was reported.[31]

Magnesium also forms heteronuclear complexes with either the d-block or p-block metals. Since the synthesis of Mg–Fe bonded complexes in 1974,[32] a number of heteronuclear complexes containing Mg–Fe, Mg–Pt, Mg–Zn and Mg–Al bonds have been reported.[33–38] The first Mg(0)–Mn(II) bonded complex was reported in 2014,[35] whose reductive reactivity towards CO_2 and H_2O has recently been examined.[39] Here we report the generation and spectroscopic characterization of $MgFe(CO)_4^-$ and $Mg_2Fe(CO)_4^-$ in the gas phase. Mass-selected infrared photodissociation spectroscopy and theoretical calculations indicate that both complexes involve an electron-sharing Mg(I)–Fe(−II) σ bond. The $Mg_2Fe(CO)_4^-$ complex involves a relatively weak covalent Mg(0)–Mg(I) σ bond.

Experimental and computational methods

The magnesium–iron carbonyl anion complexes were generated in the gas phase by a pulsed laser vaporization/supersonic expansion ion source and were detected by mass-selected infrared photodissociation spectroscopy as previously described in detail.[43] The 1064 nm fundamental of a Nd:YAG laser (Continuum, Minilite

Collaborative Innovation Center of Chemistry for Energy Materials, Department of Chemistry, Shanghai Key Laboratory of Molecular Catalysts and Innovative Materials, Fudan University Shanghai, Shanghai 200438, China.
E-mail: mfzhou@fudan.edu.cn

† Electronic supplementary information (ESI) available. See DOI: https://doi.org/10.1039/d2cp05719k

II) was applied to vaporize a magnesium metal target. The metal carbonyl complexes were produced during the laser vaporization process in a pulsed supersonic expansion of helium seeded with 10% CO containing traces of $Fe(CO)_5$ impurity at 0.7–1.2 MPa backing pressure. The anions were skimmed and analyzed by time-of-flight mass spectrometry (TOFMS). The target anions were mass-selected and decelerated to experience subsequent infrared photodissociation. An OPO/OPA system (Laser Vision) pumped by a Nd:YAG laser (Continuum Surelite EX) was employed to provide a tunable infrared laser of energy of about 0.6–1.0 mJ per pulse in the range of 1600–2200 cm^{-1}. After laser irradiation, the dissociated fragment anions together with undissociated parent anions were reaccelerated and detected by using a second colinear TOFMS instrument. The IR spectra were obtained by monitoring the dissociation efficiency as a function of the laser wavenumber. The laser wavenumber was scanned in steps of 2 cm^{-1} and the dissociation efficiency was averaged over 250 laser shots per step. The wavenumber was calibrated by the absorption spectrum of CO.

In order to analyze the IR spectra and to confirm the geometric and electronic structures of the anion complexes, quantum chemical calculations were performed. Density functional theory (DFT) calculations at the B3LYP/aug-cc-pVTZ level[44–46] using the Gaussian 09 program[47] were carried out to optimize the equilibrium geometries and to simulate the vibrational frequencies. The harmonic vibrational frequencies were scaled by a factor of 0.971, which was obtained from the ratio of experimental stretching frequency of 2143 cm^{-1} for CO and the calculated value of 2207 cm^{-1}. Mayer and Fuzzy bond orders of the most stable structures were calculated at the B3LYP/cc-pVTZ level using the B3LYP/aug-cc-pVTZ optimized geometries. Charge populations of the lowest lying structures with Hirshfeld, VDD, QTAIM and NPA at the B3LYP/aug-cc-pVTZ level were analyzed using the Multiwfn program[48] or NBO 3.0 in the Gaussian 09 program. Energy decomposition analysis with natural orbitals of chemical valence (EDA-NOCV)[49,50] was applied to study chemical bonding. The EDA-NOCV bonding analysis decomposes the instantaneous interaction energy (ΔE_{int}) among two or more fragments of a molecule into three main components: the Pauli repulsion energy (ΔE_{Pauli}), the quasi-classical electrostatic interaction energy (ΔE_{elstat}) and the orbital interaction energy (ΔE_{orb}). The total ΔE_{orb} is further partitioned into several pairwise contributions of the orbital interactions, making it possible to clarify the dominant covalent interactions and the orbitals involved. The EDA-NOCV analyses were performed at the PBE/TZ2P level with the ADF 2014 program package[51] using the B3LYP/aug-cc-pVTZ optimized geometries.

Results and discussion

The mass spectrum of the anion complexes produced by laser vaporization of a magnesium metal target in an expansion of helium seeded with 10% CO containing trace of $Fe(CO)_5$ impurity is shown in Fig. 1. Besides the peaks due to $Fe(CO)_4^-$ and $FeC(CO)_4^-$,

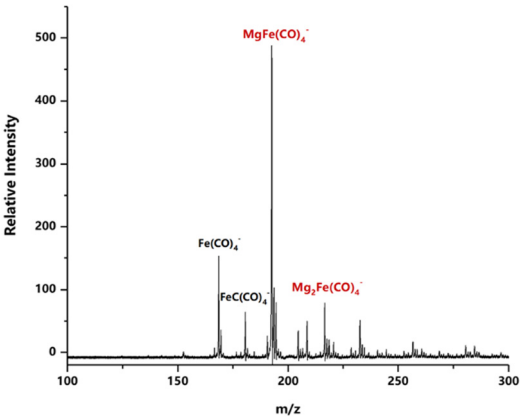

Fig. 1 The mass spectrum of the magnesium–iron carbonyl anion complexes produced by pulsed laser vaporization of a magnesium metal target in an expansion of helium seeded by 10% carbon monoxide with traces of $Fe(CO)_5$ impurity.

two intense mass peaks (m/z = 192 and 216) due to magnesium–iron carbonyl anion complexes $MgFe(CO)_4^-$ and $Mg_2Fe(CO)_4^-$ are observed. The isotopic splitting of magnesium (^{24}Mg, ^{25}Mg and ^{26}Mg) can be clearly seen (See Fig. S1, ESI†), which confirms the number of Mg atoms involved in these species. Both mass peaks remain quite intense under different experimental conditions, while the peaks of $Mg_{1,2}Fe(CO)_n^-$ with $n > 4$ are barely observed, indicating that $MgFe(CO)_4^-$ and $Mg_2Fe(CO)_4^-$ should be coordinatively saturated complexes. Both complexes are then mass-selected and subjected to infrared photodissociation. Both complexes dissociate *via* the loss of a Mg atom rather than a CO ligand in the terminal carbonyl stretching frequency region. Under focused IR laser irradiation, the dissociation efficiency of $MgFe(CO)_4^-$ is extremely low (below 1% at 1841 cm^{-1}), while that of $Mg_2Fe(CO)_4^-$ is higher (9% at 1847 cm^{-1}), suggesting that Mg–[$Fe(CO)_4^-$] is more strongly bound than Mg–[$MgFe(CO)_4^-$]. The dissociation of $MgFe(CO)_4^-$ requires multiphoton absorption. The observation of the fragmentation channel *via* the loss of a magnesium atom suggests that the $MgFe(CO)_4^-$ anion has a Mg–Fe bonded Mg–$Fe(CO)_4$ structure, in which all four CO ligands are coordinated on the Fe center. The infrared photodissociation spectra of $MgFe(CO)_4^-$ and $Mg_2Fe(CO)_4^-$ are shown in Fig. 2a and c, respectively. The spectrum of $MgFe(CO)_4^-$ exhibits two broad bands centered at 1841 and 1953 cm^{-1}, while that of $Mg_2Fe(CO)_4^-$ exhibits three bands centered at 1847, 1875 and 1959 cm^{-1}.

In order to obtain a better quality IR spectrum of the $MgFe(CO)_4^-$ anion, the $MgFe(CO)_5^-$ anion complex with the fifth CO ligand being weakly tagged is formed for infrared photodissociation. The complex dissociates quite efficiently (over 20% at 1847 cm^{-1}) using an unfocused IR laser beam *via* loss of a CO ligand, confirming that the fifth CO ligand is weakly bound. The infrared photodissociation spectrum of $MgFe(CO)_5^-$ is shown in Fig. 2b, which exhibits three intense bands at 1847, 1873 and 1955 cm^{-1}. In addition, a weak band at 2133 cm^{-1} is also observed, which is slightly red-shifted from that of free CO. This band is attributed to the absorption of the weakly bound CO

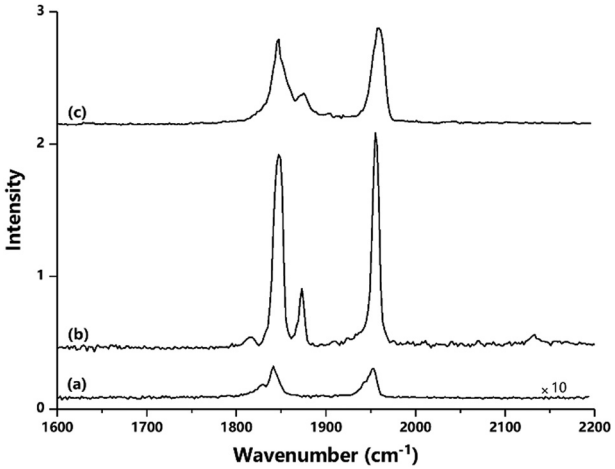

Fig. 2 The infrared photodissociation spectra of (a) $MgFe(CO)_4^-$, (b) $MgFe(CO)_5^-$ and (c) $Mg_2Fe(CO)_4^-$ in the carbonyl stretching frequency region.

ligand.[52,53] Therefore, the 1847, 1873 and 1955 cm^{-1} bands can be assigned to the vibrational fundamentals of the $MgFe(CO)_4^-$ core anion. The band positions of $MgFe(CO)_4^-$ and $Mg_2Fe(CO)_4^-$ are almost the same and the spectral patterns are similar to that of $BeFe(CO)_4^-$, which was characterized to have a Be–Fe bonded structure with C_{3v} symmetry.[12] It is worthy to mention that the bands are obviously red-shifted from those of $Fe(CO)_4^-$.[54] The carbonyl stretching frequencies of the aforementioned species are listed in Table 1.

Quantum chemical calculations are performed to validate the experimental assignments and to elucidate the structures and chemical bondings of the $MgFe(CO)_4^-$ and $Mg_2Fe(CO)_4^-$ anion complexes. The optimized geometries and relative energies at the B3LYP/aug-cc-pVTZ level for different isomers of $MgFe(CO)_4^-$ and $Mg_2Fe(CO)_4^-$ are shown in Tables S1 and S2 in the ESI,† respectively, The most stable structure of each complex with its simulated IR spectrum compared with the experimental spectrum is shown in Fig. 3. The structure of $MgFe(CO)_5^-$ with a tagging CO is shown in Fig. S4 in the ESI.† The most stable structure of $MgFe(CO)_4^-$ has a $^2A_1$ ground state and C_{3v} symmetry involving a Mg–Fe bond with all the CO ligands coordinated to the Fe center. The second isomer is predicted to lie 15.1 kcal·mol^{-1} higher in energy than the most stable structure. The most stable structure of $Mg_2Fe(CO)_4^-$ also has a $^2A_1$ ground state and C_{3v} symmetry with a Mg–Mg–Fe bonding moiety. The second and third lowest-lying isomers are

Table 1 Observed and calculated (B3LYP/aug-cc-pVTZ level) carbonyl stretching frequencies (cm^{-1}) of $MgFe(CO)_4^-$, $MgFe(CO)_5^-$, $Mg_2Fe(CO)_4^-$ and $Fe(CO)_4^-$

	Exptl.	Calcd.
$MgFe(CO)_4^-$	1841, 1953	1847, 1872, and 1938
$MgFe(CO)_5^-$	1847, 1873, 1955, and 2133	1848, 1869, 1936, and 2141
$Mg_2Fe(CO)_4^-$	1847, 1875, and 1959	1843, 1871, and 1941
$Fe(CO)_4^-$	1861, 1872, and 1978[a]	1859, 1872, and 1962

[a] Ref. 54.

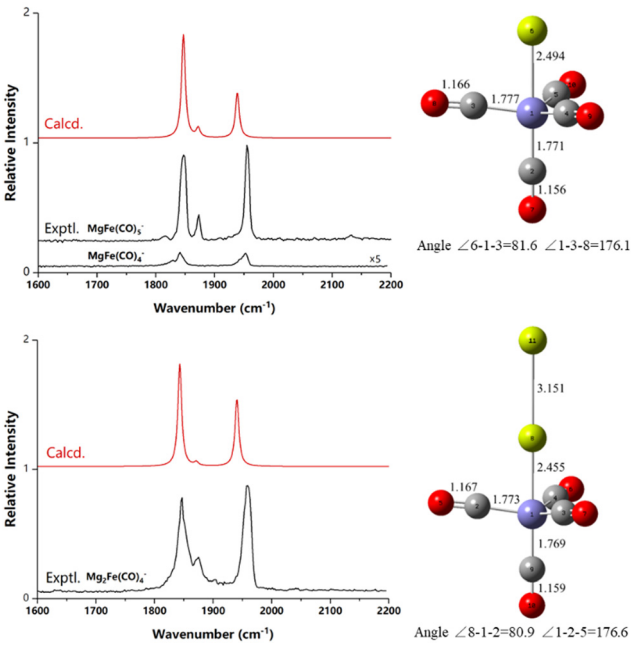

Fig. 3 Optimized equilibrium geometries of the most stable C_{3v} structures of $^2A_1$-$MgFe(CO)_4^-$ and $^2A_1$-$Mg_2Fe(CO)_4^-$ at the B3LYP/aug-cc-pVTZ level. Their simulated IR spectra are compared with the experimental spectra. The bond lengths are given in Å, and angles in degrees. Color codes for atoms: red, O; gray, C; purple, Fe; and green, Mg.

predicted to lie 5.2 and 30.9 kcal·mol^{-1} above that of the most stable structure. As shown in Fig. 3 and Fig. S2 and S3 in the ESI,† for each complex, both the band positions and IR intensities of the simulated IR spectrum of the most stable structure match very well with those of the experimental IR photodissociation spectrum, confirming that the $MgFe(CO)_4^-$ and $Mg_2Fe(CO)_4^-$ anion complexes generated in the gas phase are both in the $^2A_1$ ground state with C_{3v} symmetry, containing a heteronuclear Mg–Fe bond or a Mg–Mg–Fe bonding unit.

Besides the bands due to the CO-tagged complex, there is an additional weak band at 1815 cm^{-1} in the spectrum of $MgFe(CO)_5^-$ (Fig. 2b). This band is most likely due to another $MgFe(CO)_5^-$ isomer. Theoretical calculations predict that the most stable isomer of $MgFe(CO)_5^-$ has C_{3v} symmetry with all the CO ligands chemically bound to the metal centers (Fig. S4 in the ESI†). This structure is predicted to be about 5.4 kcal mol^{-1} more stable than the CO-tagged isomer. This isomer is expected to have much a lower IR dissociation efficiency than the tagged complex.

The calculated Mg–Fe and Mg–Mg bond distances and bond orders in the $MgFe(CO)_4^-$ and $Mg_2Fe(CO)_4^-$ anion complexes are presented in Table 2. The Mg–Fe bond distance in $MgFe(CO)_4^-$ is predicted to be 2.49 Å. This value is close to the sum of the single bond covalent radii of magnesium and iron (Mg + Fe = 2.53 Å)[55] and is much longer than that of the double bond covalent radii (Mg + Fe = 2.18 Å).[56] The Mg–Fe and Mg–Mg bond distances in $Mg_2Fe(CO)_4^-$ are calculated to be 2.46 and 3.15 Å, respectively. The latter value is much longer than the single bond covalent radii of magnesium (2.72 Å).[55]

Table 2 Calculated bond distances and bond orders of the Mg–Fe and Mg–Mg bonds in $MgFe(CO)_4^-$ and $Mg_2Fe(CO)_4^-$. The Mayer and Fuzzy bond orders are calculated at the B3LYP/cc-pVTZ level using the geometries optimized at the B3LYP/aug-cc-pVTZ level

		Bond distance (Å)	Mayer bond order	Fuzzy bond order
$MgFe(CO)_4^-$	Mg–Fe	2.494	0.73	0.82
$Mg_2Fe(CO)_4^-$	Mg–Fe	2.455	0.48	0.78
	Mg–Mg	3.151	0.57	0.75

The Mayer and Fuzzy bond orders for the Mg–Mg bond are 0.57 and 0.75, respectively, indicating a certain but weak chemical bonding between two magnesium atoms. The Mayer bond order and Fuzzy bond order share the same physical foundation although they define atomic regions in a different way, thus in general agreement.[57] The calculated bond dissociation energies (D_0) of the $MgFe(CO)_4^-$, $MgFe(CO)_5^-$ and $Mg_2Fe(CO)_4^-$ anion complexes *via* the loss of a Mg atom and a CO ligand with respect to the minimum energy structures of the fragments are shown in Table S3 in the ESI.† D_0(–Mg) is much lower than D_0(–CO) for both $MgFe(CO)_4^-$ and $Mg_2Fe(CO)_4^-$, in agreement with the experimental observation that both complexes dissociate *via* the loss of a Mg atom rather than a CO ligand. The D_0(–Mg) value of $Mg_2Fe(CO)_4^-$ is calculated to be only 2.5 kcal·mol^{-1}, comparable to the weak covalent Be–Be bond in the Be_2 molecule (2.7 kcal·mol^{-1}),[58] suggesting a weak Mg–Mg bond.

Population analyses are performed for $MgFe(CO)_4^-$ and $Mg_2Fe(CO)_4^-$ and the values are listed in Tables S4 and S5 in the ESI.† The contours of the frontier canonical Kohn–Sham valence molecular orbitals (MOs) are shown in Fig. 4 and the AO contributions are listed in Tables S6 and S7 in the ESI.† The results show that the negative charge of $MgFe(CO)_4^-$ is mainly located on the $Fe(CO)_4$ moiety (Table S4, ESI†). The SOMO ($11a_1$) of $MgFe(CO)_4^-$ composed of 64.9% Mg (45.9% 3s + 19.0% 3p) and 21.3% Fe is roughly Mg–Fe non-bonding in character. It is bonding between the Mg 3p and Fe 3d orbitals but is antibonding between the Mg 3s and Fe 3d orbitals. The HOMO-2 ($10a_1$) is a σ-type Mg–Fe bonding MO formed by the Mg 3s AO and the SOMO of $Fe(CO)_4^-$. The HOMO-1 ($9e_1$) and HOMO-3 ($8e_1$) are both π-type MOs of the $Fe(CO)_4^-$ moiety with negligible contribution from Mg. This bonding analysis indicates that $MgFe(CO)_4^-$ contains a Mg–Fe σ bond.

In order to quantitatively understand the bonding interactions between Mg and Fe in the $MgFe(CO)_4^-$ anion complex, energy decomposition analysis with natural orbital for chemical valence (EDA-NOCV) is performed. Table 3 shows the numerical results of the EDA-NOCV calculations using either Mg in the ^3P ($3s^13p^1$) excited state and $Fe(CO)_4^-$ in the $^2A_1$ ground state or Mg^+ in the ^2P ($3s^03p^1$) excited state and $Fe(CO)_4^{2-}$ in the $^1A_1$ ground state as interaction fragments. The former describes the HOMO-2 as electron-sharing σ bonding, while the latter describes it as $Mg^+ \leftarrow Fe(CO)_4^{2-}$ dative σ bonding. According to the results listed in Table 3, the former description with fragments Mg + $Fe(CO)_4^-$ leads to a much smaller value for the orbital interaction ΔE_{orb} than

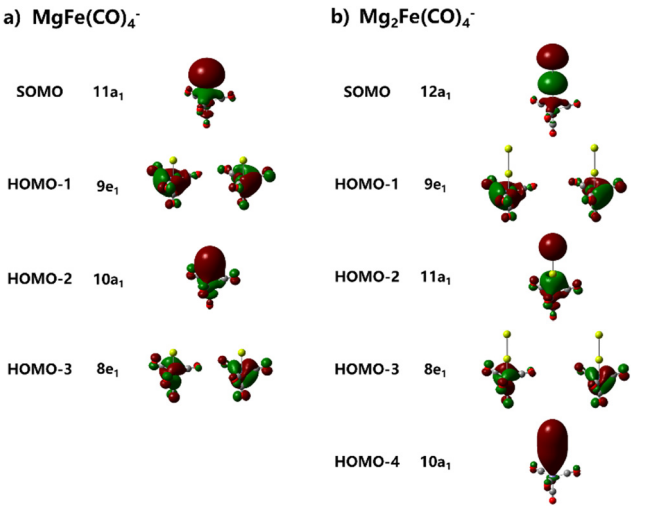

Fig. 4 The contours of the frontier Kohn–Sham canonical valence MOs (isosurface = 0.03 a.u.) at the B3LYP/aug-cc-pVTZ level of the most stable C_{3v} structure of (a) $^2A_1$-$MgFe(CO)_4^-$ and (b) $^2A_1$-$Mg_2Fe(CO)_4^-$. Color codes for atoms: red, O; gray, C; purple, Fe; and green, Mg.

Table 3 EDA-NOCV results at the PBE/TZ2P level of $^2A_1$-$MgFe(CO)_4^-$ using (a) Mg in the ^3P ($3s^13p^1$) excited state and $Fe(CO)_4^-$ in the $^2A_1$ ground state and (b) Mg^+ in the ^2P ($3s^03p^1$) excited state and $Fe(CO)_4^{2-}$ in the $^1A_1$ ground state as interaction fragments. Energy values are given in kcal·mol^{-1}

Energy	Mg (^{3}P) + $Fe(CO)_4^-$ ($^2A_1$)	Mg^+ (^{2}P) + $Fe(CO)_4^{2-}$ ($^1A_1$)
ΔE_{int}	−92.2	−364.3
ΔE_{Pauli}	176.4	136.3
ΔE_{elstat}[a]	−165.8 (61.7%)	−346.3 (69.2%)
ΔE_{orb}[a]	−102.8 (38.3%)	−154.3 (30.8%)
$\Delta E_{orb(\sigma)}$[b]	−91.4 (88.9%)	−116.2 (75.3%)
$\Delta E_{orb(\pi1)}$[b]	−4.1 (4.0%)	−6.8 (4.4%)
$\Delta E_{orb(\pi2)}$[b]	−4.1 (4.0%)	−6.8 (4.4%)
$\Delta E_{orb(rest)}$[b]	−3.2 (3.1%)	−24.5 (15.9%)

[a] The values in parentheses give the percentage contribution to the total attractive interactions $\Delta E_{elstat} + \Delta E_{orb}$. [b] The values in parentheses give the percentage contribution to the total orbital interactions ΔE_{orb}.

the description using fragments $Mg^+ + Fe(CO)_4^{2-}$, which indicates that the former moieties should be chosen for analyzing the interatomic interactions.[59–61] The calculated values indicate that the bonding between Mg and $Fe(CO)_4^-$ has a higher electrostatic character (61.7%) than covalent character (38.3%). The decomposition of ΔE_{orb} suggests that the dominant orbital interaction is a σ-type electron-sharing bonding (See Table S8, ESI†), which contributes 88.9% of the covalent interaction. The two Mg ← $Fe(CO)_4^-$ dative π bonding components are really weak, each having a calculated interaction energy of only 4.1 kcal·mol^{-1}, which is to some extent negligible for the Mg–Fe bonding.

The $Mg_2Fe(CO)_4^-$ anion can be recognized as $MgFe(CO)_4^-$ being further bonded with another magnesium atom, forming a Mg–Mg bond. Population analyses indicate that the negative charge is largely located at the $Fe(CO)_4$ moiety, with the middle Mg atom being partially positively charged and the terminal Mg

atom being essentially neutral. According to the contours of MOs (Fig. 4b) and the contributions of AOs (Table S7, ESI†), the SOMO, HOMO-2 and HOMO-4 are all σ-type MOs. The SOMO ($12a_1$) with composition of 39.4% terminal Mg, 39.1% middle Mg and 12.7% Fe is more or less Mg–Mg non-bonding in character as there is significant contribution from the 3p AOs of the Mg atoms. It is antibonding between the 3s AOs of Mg but is bonding between the Mg 3p AOs. The HOMO-4 ($10a_1$), mainly formed by the 3s AOs of the Mg atoms, is a Mg–Mg bonding MO. The other MOs are not involved in Mg–Mg bonding.

The numerical results of the EDA-NOCV calculations of $Mg_2Fe(CO)_4^-$ are listed in Table 4. The fragments Mg ($3s^13p^1$, ^3P) + $MgFe(CO)_4^-$ ($^2A_1$) give a much smaller value for the orbital interaction ΔE_{orb} than using the Mg^+ ($3s^03p^1$, ^2P) + $MgFe(CO)_4^{2-}$ ($^1A_1$) fragments. Therefore, the former fragments should be chosen for analyzing the interatomic interactions. Under this description, the covalent interaction ΔE_{orb} (52.9%) is slightly higher than the electrostatic character ΔE_{elstat} (47.1%). The decomposition of ΔE_{orb} into pairwise orbital interactions suggests that there is only one major component to the total orbital interactions, which provides 95.3% of ΔE_{orb}. This orbital interaction can be identified with the help of the associated deformation densities (See Table S9, ESI†) and the fragment orbitals to the electron-sharing σ bonding interaction between the two fragments. The calculated instantaneous interaction energy (ΔE_{int}) of 73.8 kcal·mol^{-1} is significantly larger than the bond dissociation energy of 2.5 kcal·mol^{-1}. The ΔE_{int} is different from and should not be confused with the bond dissociation energy D_0. The fragments used in the EDA-NOCV analysis are not in their ground state or relaxed geometries.[62] Based on the aforementioned bonding analyses, the Mg–Mg bonding contains apparent covalent interaction despite the very long bond distance and small bond dissociation energy.

To assess the potential single-reference nature of the electronic structures of both complexes, additional single-point multi-configurational SCF calculations using the complete-active-space self-consistent field (CASSCF) method[63] at the DFT optimized geometries are performed. The CASSCF calculations using 7 electrons in 9 orbitals for $MgFe(CO)_4^-$ and 9 electrons in 9 orbitals for $Mg_2Fe(CO)_4^-$ reveal that both complexes do not have significant multi-reference features. The major configuration has a weight of about 85% for both complexes.

It is meaningful to clarify the valence of Mg in the $MgFe(CO)_4^-$ and $Mg_2Fe(CO)_4^-$ anion complexes. Although the Mg–Fe bonding in $MgFe(CO)_4^-$ is better described by using the neutral Mg (^3P) atom and the $Fe(CO)_4^-$ ($^2A_1$) anion as interaction fragments, the electron-sharing Mg–Fe σ bond is apparently a polarized one. The NOCV eigenvalue of the deformation densities ν_k, which indicates the size of charge migration, is larger for the α term than for the β term (See Table S8, ESI†), suggesting electron density migration from Mg to Fe in the Mg–Fe σ bond. The calculated charge on Mg is +0.52 (AIM) or +0.47 (NPA), also indicating electron migration from Mg to Fe during the bonding. These results define the valence of Mg as +1 in the $MgFe(CO)_4^-$ anion. The Mg–Mg bonding in the $Mg_2Fe(CO)_4^-$ anion is appropriately described using the neutral Mg (^3P) atom and the $MgFe(CO)_4^-$ ($^2A_1$) anion as interaction fragments. According to the deformation densities ν_k (Table S9, ESI†), the terminal Mg atom gains only slightly more electron density than $MgFe(CO)_4^-$ during electron-sharing σ bonding. The calculated charge of the terminal Mg (−0.11 with AIM or −0.02 with NPA) is very close to zero. The valence of the terminal Mg can thus be recognized as zero, suggesting a Mg(0)–Mg(I) bond in the $Mg_2Fe(CO)_4^-$ anion. The Mg(I)–Mg(I) bond is well recognized in homonuclear complexes since the first report in 2007,[14] but the Mg(0)–Mg(I) bond is rarely reported. A recent progress in low oxidation state alkaline-earth metal chemistry is the isolation of the first Mg(0) complex containing a $Mg_2Na_2^{2+}$ cluster stabilized by superbulky, monoanionic, β-diketiminate ligands. A related complex containing a Mg(I)–Mg(0)–Mg(I) bonding unit was also reported, in which the two Mg(0)–Mg(I) bonds were determined to have an equal distance of 2.8876(5) Å.[31] The gas-phase complex $Mg_2Fe(CO)_4^-$ with a Mg(0)–Mg(I) bond reported here contains no bulky group, which is predicted to have a much longer Mg(0)–Mg(I) bond distance of 3.15 Å.

The lack of significant π bonding distinguishes Mg–Fe bonding from the Be–Fe bonding in $BeFe(CO)_4^-$, which contains weak but non-negligible dative π bonding interactions between the Be $2p_\pi$ AOs and the $Fe(CO)_4^-$ π MOs.[12] This can be attributed to the different atomic radius of Be and Mg, which leads to distinct efficiency of overlapping between the metal p_π AOs and the occupied $Fe(CO)_4^-$ π orbitals. The impact of π bonding between the metal atom and the $Fe(CO)_4^-$ fragment is reflected in the carbonyl stretching frequencies. It is well known that the metal to CO 2π* backdonation bonding weakens the CO bond and results in a red-shift of the carbonyl stretching frequency with respect to free CO.[64–66] The MOs of the $Fe(CO)_4^-$ fragment involved in bonding with the Be or Mg atoms all comprise Fe → CO π backdonation bonding interactions (Fig. S5, ESI†). The carbonyl stretching frequencies of $BeFe(CO)_4^-$ observed at 1872, 1899 and 1978 cm^{-1} are equal or blue-shifted from the corresponding modes of free $Fe(CO)_4^-$ at 1861, 1872 and 1978 cm^{-1},[54] which can be understood by the

Table 4 EDA-NOCV results at the PBE/TZ2P level of $^2A_1$-$Mg_2Fe(CO)_4^-$ using (a) Mg in the ^3P ($3s^13p^1$) excited state and $MgFe(CO)_4^-$ in the $^2A_1$ ground state and (b) Mg^+ in the ^2P ($3s^03p^1$) excited state and $MgFe(CO)_4^{2-}$ in the $^1A_1$ ground state as interaction fragments. Energy values are given in kcal·mol^{-1}

Energy	Mg (^3P) + $MgFe(CO)_4^-$ ($^2A_1$)	Mg^+ (^2P) + $MgFe(CO)_4^{2-}$ ($^1A_1$)
ΔE_{int}	−73.8	−338.6
ΔE_{Pauli}	23.0	30.5
ΔE_{elstat}[a]	−45.6 (47.1%)	−217.7 (59.0%)
ΔE_{orb}[a]	−51.2 (52.9%)	−151.4 (41.0%)
$\Delta E_{orb(\sigma)}$[b]	−48.8 (95.3%)	−139.2 (91.9%)
$\Delta E_{orb(rest)}$[b]	−2.4 (4.7%)	−12.2 (8.1%)

[a] The values in parentheses give the percentage contribution to the total attractive interactions $\Delta E_{elstat} + \Delta E_{orb}$. [b] The values in parentheses give the percentage contribution to the total orbital interactions ΔE_{orb}.

impact of π bonding. The π bonding interactions between the vacant Be $2p_{x/y}$ AOs and the occupied $8e_1$ MOs of $Fe(CO)_4^-$ induce electron density migration from $Fe(CO)_4^-$ to Be, which weakens the Fe → CO π-backdonation bonding and leads to a blue-shift of the carbonyl stretching frequencies. In the case of $MgFe(CO)_4^-$, the Fe → Mg π bonding is much weaker than that in $BeFe(CO)_4^-$. The electron density migration from Mg to $Fe(CO)_4^-$ due to the highly polarized σ bonding interaction between Mg and Fe enhances the Fe → CO π-backdonation bonding and leads to a red-shift of the carbonyl stretching frequencies. The carbonyl stretching frequencies of $MgFe(CO)_4^-$ at 1847, 1873 and 1955 cm^{-1} are all red-shifted from those of free $Fe(CO)_4^-$.[54]

Conclusions

The heteronuclear magnesium–iron carbonyl anion complexes $MgFe(CO)_4^-$ and $Mg_2Fe(CO)_4^-$ have been produced in the gas phase. Infrared photodissociation spectroscopy combined with quantum chemical calculations confirm that both complexes have a $^2A_1$ ground state with C_{3v} symmetry containing a Mg–Fe bond or a Mg–Mg–Fe bond unit. Bonding analyses indicate that the Mg–Fe bonding is dominated by electron-sharing σ interactions with negligible π bonding interactions, which is different from the Be–Fe bonding in $BeFe(CO)_4^-$. The $Mg_2Fe(CO)_4^-$ anion contains a Mg(0)–Mg(I) bond, which contains apparent covalent electron-sharing σ interaction despite the very long bond distance and small bond dissociation energy. The electron density migration from Mg to $Fe(CO)_4^-$ due to the highly polarized σ bonding interaction between Mg and Fe enhances the Fe → CO π-backdonation bonding and leads to a red-shift of the carbonyl stretching frequencies.

Conflicts of interest

There are no conflicts to declare.

Acknowledgements

The experimental work was financially supported by the National Natural Science Foundation of China (grant number 21688102). The authors thank Dr Wei Fang for performing the single point multi-reference calculations.

Notes and references

1 P. A. Lindahl, *J. Inorg. Biochem.*, 2012, **106**, 172–178.
2 I. G. Powers and C. Uyeda, *ACS Catal.*, 2016, **7**, 936–958.
3 J. F. Berry and C. C. Lu, *Inorg. Chem.*, 2017, **56**, 7577–7581.
4 J. A. Chipman and J. F. Berry, *Chem. Rev.*, 2020, **120**, 2409–2447.
5 Q. R. Wang, S. H. Brooks, T. C. Liu and N. C. Tomson, *Chem. Commun.*, 2021, **57**, 2839–2853.
6 A. Kondinski, *Nanoscale*, 2021, **13**, 13574–13592.
7 M. P. Blake, N. Kaltsoyannis and P. Mountford, *J. Am. Chem. Soc.*, 2015, **137**, 12352–12368.
8 S. S. Rohman, C. Kashyap, S. S. Ullah, A. K. Guha, L. J. Mazumder and P. K. Sharma, *ChemPhysChem*, 2019, **20**, 516–518.
9 G. J. Wang, Y. Y. Zhou, X. Y. Jin, J. Y. Jin and M. F. Zhou, *Angew. Chem., Int. Ed.*, 2021, **60**, 1651–1655.
10 H. Braunschweig, K. Gruss and K. Radacki, *Angew. Chem., Int. Ed.*, 2009, **48**, 4239–4241.
11 A. Paparo, C. D. Smith and C. Jones, *Angew. Chem., Int. Ed.*, 2019, **58**, 11459–11463.
12 G. J. Wang, J. Zhao, H. S. Hu, J. Li and M. F. Zhou, *Angew. Chem., Int. Ed.*, 2021, **60**, 9334–9338.
13 P. M. Chapple, J. Cartron, G. Hamdoun, S. Kahlal, M. Cordier, H. Oulyadi, J. F. Carpentier, J. Y. Saillard and Y. Sarazin, *Chem. Sci.*, 2021, **12**, 7098–7114.
14 S. P. Green, C. Jones and A. Stasch, *Science*, 2007, **318**, 1754–1757.
15 A. Stasch and C. Jones, *Dalton Trans.*, 2011, **40**, 5659–5672.
16 M. Ma, A. Stasch and C. Jones, *Chem. – Eur. J.*, 2012, **18**, 10669–10676.
17 A. Stasch, *Angew. Chem., Int. Ed.*, 2014, **53**, 10200–10203.
18 C. Bakewell, A. J. White and M. R. Crimmin, *J. Am. Chem. Soc.*, 2016, **138**, 12763–12766.
19 C. Jones, *Nat. Rev. Chem.*, 2017, **1**, 1–9.
20 A. J. Boutland, A. Carroll, C. A. Lamsfus, A. Stasch, L. Maron and C. Jones, *J. Am. Chem. Soc.*, 2017, **139**, 18190–18193.
21 G. Coates, B. J. Ward, C. Bakewell, A. J. P. White and M. R. Crimmin, *Chem. – Eur. J.*, 2018, **24**, 16282–16286.
22 D. D. L. Jones, I. Douair, L. Maron and C. Jones, *Angew. Chem., Int. Ed.*, 2021, **60**, 7087–7092.
23 Y. J. Xue, J. J. Wang, Y. L. Shi, W. H. Xu, Y. X. Zhao, B. A. Wu and X. J. Yang, *Dalton Trans.*, 2022, **51**, 4394–4399.
24 C. Bakewell, B. J. Ward, A. J. P. White and M. R. Crimmin, *Chem. Sci.*, 2018, **9**, 2348–2356.
25 A. Paparo, K. Yuvaraj, A. J. R. Matthews, I. Douair, L. Maron and C. Jones, *Angew. Chem., Int. Ed.*, 2021, **60**, 630–634.
26 Y. P. Cai, S. J. Jiang, L. Q. Dong and X. Xu, *Dalton Trans.*, 2022, **51**, 3817–3827.
27 J. Overgaard, C. Jones, A. Stasch and B. B. Iversen, *J. Am. Chem. Soc.*, 2009, **131**, 4208–4209.
28 J. A. Platts, J. Overgaard, C. Jones, B. B. Iversen and A. Stasch, *J. Phys. Chem. A*, 2011, **115**, 194–200.
29 C. Jones, *Commun. Chem.*, 2020, **3**, 159–162.
30 H. Y. Liu, R. J. Schwamm, S. E. Neale, M. S. Hill, C. L. McMullin and M. F. Mahon, *J. Am. Chem. Soc.*, 2021, **143**, 17851–17856.
31 B. Rosch, T. X. Gentner, J. Eyselein, J. Langer, H. Elsen and S. Harder, *Nature*, 2021, **592**, 717–721.
32 H. Felkin, P. J. Knowles, B. Meunier, A. Mitschle, L. Ricard and R. Weiss, *J. Am. Chem. Soc.*, 1974, **2**, 44.
33 K. Jonas, G. Koepe and C. Kruger, *Angew. Chem., Int. Ed. Engl.*, 1986, **25**, 923–925.
34 M. P. Blake, N. Kaltsoyannis and P. Mountford, *Chem. Commun.*, 2013, **49**, 3315–3317.
35 J. Hicks, C. E. Hoyer, B. Moubaraki, G. Li Manni, E. Carter, D. M. Murphy, K. S. Murray, L. Gagliardi and C. Jones, *J. Am. Chem. Soc.*, 2014, **136**, 5283–5286.
36 R. Green, A. C. Walker, M. P. Blake and P. Mountford, *Polyhedron*, 2016, **116**, 64–75.
37 C. Birchall, G. J. Moxey, J. McMaster, A. J. Blake, W. Lewis and D. L. Kays, *Inorg. Chim. Acta*, 2017, **458**, 97–100.

38 J. A. Kelly, J. Gramuller, R. M. Gschwind and R. Wolf, *Dalton Trans.*, 2021, **50**, 13985–13992.
39 J. Hicks, M. Juckel and C. Jones, *Main Group Met. Chem.*, 2021, **44**, 250–255.
40 F. G. Baddour, A. S. Hyre, J. L. Guillet, D. Pascual, J. M. Lopez-de-Luzuriaga, T. M. Alam, J. W. Bacon and L. H. Doerrer, *Inorg. Chem.*, 2017, **56**, 452–469.
41 P. Stegner, C. Farber, J. Oetzel, U. Siemeling, M. Wiesinger, J. Langer, S. Pan, N. Holzmann, G. Frenking, U. Albold, B. Sarkar and S. Harder, *Angew. Chem., Int. Ed.*, 2020, **59**, 14615–14620.
42 X. Y. Jin, Y. N. Bai, Y. Y. Zhou, G. J. Wang, L. L. Zhao, M. F. Zhou and G. Frenking, *Angew. Chem., Int. Ed.*, 2021, **60**, 13865–13870.
43 G. J. Wang, C. X. Chi, X. P. Xing, C. F. Ding and M. F. Zhou, *Sci. China: Chem.*, 2013, **57**, 172–177.
44 A. D. Becke, *J. Chem. Phys.*, 1993, **98**, 5648–5652.
45 C. Lee, W. Yang and R. G. Parr, *Phys. Rev. B: Condens. Matter Mater. Phys.*, 1988, **37**, 785–789.
46 D. E. Woon and T. H. Dunning, *J. Chem. Phys.*, 1994, **100**, 2975–2988.
47 M. J. Frisch, G. W. Trucks, H. B. Schlegel, G. E. Scuseria, M. A. Robb, G. Cheeseman, J. R. Scalmani, V. Barone, B. Mennucci, G. A. Petersson, H. Nakatsuji, M. Caricato, X. Li, H. P. Hratchian, A. F. Izmaylov, J. Bloino, G. Zheng, J. L. Sonnenberg, M. Hada, M. Ehara, K. Toyota, R. Fukuda, J. Hasegawa, M. Ishida, T. Nakajima, Y. Honda, O. Kitao, H. Nakai, T. Vreven, J. A. Montgomery Jr., J. E. Peralta, F. Ogliaro, M. Bearpark, J. J. Heyd, E. Brothers, K. N. Kudin, V. N. Staroverov, R. Kobayashi, J. Nomand, K. Raghavachari, A. Rendell, J. C. Burant, S. S. Iyengar, J. Tomasi, M. Cossi, N. Rega, J. M. Millam, M. Klene, J. E. Knox, J. B. Cross, V. Bakken, C. Adamo, J. Jaramillo, R. Gomperts, R. E. Stratmann, O. Yazyev, A. J. Austin, R. Cammi, C. Pomelli, J. W. Ochterski, R. L. Martin, K. Morokuma, V. G. Zakrzewski, G. A. Voth, P. Salvador, J. J. Dannenberg, S. Dapprich, A. D. Daniels, O. Farkas, J. B. Foresman, J. V. Ortiz, J. Cioslowski and D. J. Fox, *Gaussian 09, Revision D.01*, Gaussian, Inc., Wallingford CT, 2013.
48 T. Lu and F. W. Chen, *J. Comput. Chem.*, 2012, **33**, 580–592.
49 A. Michalak, M. Mitoraj and T. Ziegler, *J. Phys. Chem. A*, 2008, **112**, 1933–1939.
50 M. P. Mitoraj, A. Michalak and T. Ziegler, *J. Chem. Theory Comput.*, 2009, **5**, 962–975.
51 G. te Velde, F. M. Bickelhaupt, E. J. Baerends, C. F. Guerra, S. J. A. Van Gisbergen, J. G. Snijders and T. Ziegler, *J. Comput. Chem.*, 2001, **22**, 931–967.
52 G. J. Wang and M. F. Zhou, *Chin. J. Chem. Phys.*, 2018, **31**, 1–11.
53 A. M. Ricks, Z. E. Reed and M. A. Duncan, *J. Mol. Spectrosc.*, 2011, **266**, 63–74.
54 G. J. Wang, C. X. Chi, J. M. Cui, X. P. Xing and M. F. Zhou, *J. Phys. Chem. A*, 2012, **116**, 2484–2489.
55 P. Pyykko and M. Atsumi, *Chem. – Eur. J.*, 2009, **15**, 186–197.
56 P. Pyykko and M. Atsumi, *Chem. – Eur. J.*, 2009, **15**, 12770–12779.
57 E. Matito, J. Poater, M. Sola, M. Duran and P. Salvador, *J. Phys. Chem. A*, 2005, **109**, 9904–9910.
58 J. M. Merritt, V. E. Bondybey and M. C. Heaven, *Science*, 2009, **324**, 1548–1551.
59 M. F. Zhou and G. Frenking, *Acc. Chem. Res.*, 2021, **54**, 3071–3082.
60 L. L. Zhao, M. von Hopffgarten, D. M. Andrada and G. Frenking, *Wiley Interdiscip. Rev.: Comput. Mol. Sci.*, 2017, **8**, e1345.
61 R. Saha, S. Pan, G. Merino and P. K. Chattaraj, *Angew. Chem., Int. Ed.*, 2019, **58**, 8372–8377.
62 L. L. Zhao, M. Hermann, W. H. E. Schwarz and G. Frenking, *Nat. Rev. Chem.*, 2019, **3**, 48–63.
63 M. W. Schmidt and M. S. Gordon, *Annu. Rev. Phys. Chem.*, 1998, **49**, 233–266.
64 G. Frenking and N. Frohlich, *Chem. Rev.*, 2000, **100**, 717–774.
65 M. F. Zhou, L. Andrews and C. W. Bauschlicher, *Chem. Rev.*, 2001, **101**, 1931–1961.
66 M. H. Chen, Q. N. Zhang, M. F. Zhou, D. M. Andrada and G. Frenking, *Angew. Chem., Int. Ed.*, 2015, **54**, 124–128.